A Gulf Stream Model and an Altimetry Assimilation Scheme

GEORGE L. MELLOR AND TAL EZER

Program in Atmospheric and Oceanic Sciences, Princeton University, Princeton, New Jersey

A continuous data assimilation scheme and a multilayer, primitive equation, numerical model are described. The model is an eddy-resolving, coastal ocean model that has been extended to include the Gulf Stream region. It has complete thermohaline dynamics, a bottom-following, sigma, vertical coordinate system, and a coastal-following, curvilinear orthogonal, horizontal coordinate system. Calculated model fields are used to provide a model climatology and correlations between subsurface temperature and salinity anomalies and surface elevation anomalies. An optimal interpolation method, the surface to subsurface correlations, and estimated model and data errors are the basis of the assimilation technique. Altimetry anomaly data extracted from the model calculations according to the Geosat orbital schedule are used to test the assimilation scheme and to provide nowcasts and forecasts. Sensitivity studies are performed to test the effects of various parameters of the scheme. It is found that the scheme is less efficient in the shallow continental shelf area than in the deeper regions of the model. The results show significant nowcast skill, with area-averaged rms error for surface elevation and subsurface properties of about 40–50% of the corresponding error of the unassimilated case. Good forecast skill, better than persistence, is demonstrated for 10–20 days; there is little skill after 30–40 days. Increasing the density of the satellite altimetry data (especially by decreasing the separation distance between tracks) should decrease the nowcast rms error to about 15% and improve the forecast.

1. INTRODUCTION

Data assimilation into numerical ocean models is now an active field of research. Attention has been directed toward the use of satellite altimetry data since it promises continuous, global coverage. Most of the research to date has involved numerical ocean models with either very few layers [*Kindle*, 1986] or quasi-geostrophic dynamics [*Holland and Malanotte-Rizzoli*, 1989; *Robinson et al.*, 1988, 1989; *Verron*, 1990; *White et al.*, 1990a, b, c]. The virtues of these models are that they are simple, they do not require large computational resources, and they can be used efficiently to research assimilation concepts and techniques. On the other hand, these models generally lack some degree of realism. For example, they inaccurately represent the important large topographical variability of the coastal regions, or they do not directly include temperature and salinity as prognostic variables. An exception is the study by *Derber and Rosati* [1989], who assimilated temperature profile data from hydrocasts into a primitive equation model. *Malanotte-Rizzoli et al.* [1989] also used a primitive equation model (but without bottom topography) to explore sensitivity to the choice of variables used in initialization and assimilation.

Primitive equation models may fall short of providing a realistic climatology. In the North Atlantic, Gulf Stream separation has been a problem [e.g., *Thompson and Schmitz*, 1989]; models tend to separate north of Cape Hatteras. However, in the long run it is probable that good nowcasts and forecasts will partially depend on the capabilities of the numerical model to generate realistic climatologies and realistic statistics at scales comparable to the Rossby radius.

Data assimilation schemes vary. *Robinson et al.* [1988, 1989] primarily use satellite sea surface temperature (SST) fields to locate the Gulf Stream and mesoscale eddies. They

then construct predetermined "feature models," in particular, subsurface quasi-geostrophic stream function anomalies; outside of the anomaly regions, velocities are null. *Spall and Robinson* [1990] provide an interesting comparison between multilevel, primitive equation calculations with quasi-geostrophic calculations wherein both models are initialized with SST and subsurface feature model information. *Holland and Malanotte-Rizzoli* [1989] use a "nudging" technique whereby surrogate altimetry data, obtained from a model control run, were interpolated to model time step intervals and the error between the surrogate data and the model data became a source term for the vorticity equation in the upper layer of their three-layer models. *White et al.* [1990c] use a simple optimal interpolation method to assimilate altimetry data into the upper layer stream function of a three-layer non-eddy-resolving model. Note that the latter feature will fail if the vertical resolution is indefinitely refined as noted by *Berry and Marshall* [1989].

In the present study we use a realistic primitive equation model which has a bottom-following, vertical sigma coordinate system and a coastal-following, horizontal curvilinear coordinate system. Temperature, salinity, velocity, and surface elevation are prognostic variables. A 1-year run of the model provides a model climatology, other model statistics, and correlations between subsurface property anomalies and surface elevation. This information is combined with an optimal interpolation scheme to assimilate altimetric surface elevation data.

The plan of this paper is first to describe the dynamic model in section 2 and some of its statistical characteristics in section 3. Then, in sections 4 and 5 we obtain correlations between surface elevation and subsurface properties followed by a direct nowcast/forecast application for the case where complete areal coverage of elevation data is available. In section 6 the elevation data are subsampled according to the Geosat orbital schedule of ascending and descending tracks, and, in that context, the data assimilation scheme is described. Next, sensitivity to parameters of the assimilation

scheme is evaluated in section 7. Finally, the nowcast/forecast skill of the model and assimilation scheme is evaluated in section 8. Model calculations provide a surrogate "true" ocean or control ocean which also supplies surrogate altimetry track data for assimilation. The assimilated model is compared with the control ocean, and rms errors for surface elevation and subsurface properties are obtained.

2. THE OCEAN MODEL

The ocean model has been previously described in the literature [*Blumberg and Mellor*, 1983, 1987; *Oey et al.*, 1985a, b; *Galperin and Mellor*, 1990a, b]. We briefly note here that it is a sigma coordinate model; it has a free surface and a split mode time step. It solves the following equations for the ocean velocity $U_i = (U, V, W)$, potential temperature T, and salinity S:

$$\partial U_i / \partial x_i = 0 \tag{1}$$

$$\frac{\partial}{\partial t} (U, V) + \frac{\partial}{\partial x_i} [U_i(U, V)] + f(-V, U) = -\frac{1}{\rho_0} \left[\frac{\partial p}{\partial x}, \frac{\partial p}{\partial y} \right]$$

$$+ \frac{\partial}{\partial z} \left[K_M \frac{\partial}{\partial z} (U, V) \right] + (F_U, F_V) \tag{2}$$

$$\frac{\partial T}{\partial t} + \frac{\partial}{\partial x_i} (U_i T) = \frac{\partial}{\partial z} \left[K_H \frac{\partial T}{\partial z} \right] + F_T \tag{3}$$

$$\frac{\partial S}{\partial t} + \frac{\partial}{\partial x_i} (U_i S) = \frac{\partial}{\partial z} \left[K_H \frac{\partial S}{\partial z} \right] + F_S \tag{4}$$

The hydrostatic approximation yields

$$\frac{p}{\rho_0} = g(\eta - z) + \int_z^\eta \frac{\rho - \rho_0}{\rho_0} g \, dz \tag{5}$$

where $\rho = \rho(T, S, p)$, η is the free surface elevation, and ρ_0 is a reference density. The equations, after transformation to a sigma coordinate system ($\sigma = (z - \eta)/(H + \eta)$ where $H(x, y)$ is the bottom topography), can be found in the papers cited above. In all previous applications the turbulence closure submodel of *Mellor and Yamada* [1982] was embedded in the numerical model and generally provides the vertical mixing coefficients K_M and K_H. However, in this paper we deemphasize the surface mixed layer properties, and indeed, with 11 layers the mixed layer is only marginally resolved; we have therefore disabled the closure submodel and set K_M and K_H equal to 0.02 m^2 s^{-1} above depths of 50 m and equal to 2×10^{-5} below 50 m. We use a Smagorinsky horizontal diffusion formulation to evaluate the horizontal diffusion terms, (F_U, F_V), F_T and F_S in (2), (3), and (4), respectively. Further aspects of the horizontal diffusion associated with the sigma coordinate system are considered by *Mellor and Blumberg* [1985].

The model uses a curvilinear orthogonal grid shown in Figure 1a, and the bottom topography is in Figure 1b. The model may be considered to be a coastal ocean model which has been extended seaward to include the Gulf Stream. The horizontal grid contains 45 × 121 points. The grid elements are variable; in the central Gulf Stream region, northeast of Cape Hatteras, typical along- and cross-stream grid sizes are

17 km and 22 km, respectively. There are 12 sigma levels in the vertical.

The total transports in and out of the model are fixed such that 30 sverdrups (Sv) enter at the Florida Straits and 40 Sv enter along the northern continental slope near 43°N [*Mellor et al.*, 1982; *Richardson*, 1985; *Hogg et al.*, 1986]. An additional 30 Sv are distributed along the model's southeastern boundary from 27°N to 32°N such that the vertically averaged inflow velocity is constant. The total of 100 Sv is allowed to exit the domain on the eastern boundary between 36°N and 39°N. These inflow/outflow locations are identified in Figure 1a. Internal velocities on most of the open lateral boundaries are governed by the Sommerfeld radiation condition (using a constant phase velocity approximately equal to that of the first baroclinic mode) and are therefore free to adjust geostrophically to the density field. The exceptions are the northern slope flow, where the internal inflow velocity is fixed and is approximated as a barotropic flow, and the Florida Straits flow which is prescribed according to the Subtropical Atlantic Climate Studies (STACS) measurements [*Leaman et al.*, 1987].

The surface boundary conditions are zero heat and salinity flux and steady climatological wind stress; however, the latter are not important to the dynamics of this limited region. At the lateral boundaries, temperature and salinity are upwinded such that boundary data are used only if the flow is into the model domain. The boundary data are taken from the climatology discussed above except on the Florida Straits where, again, STACS data are used. The model is initialized with climatological temperatures and salinities analyzed by *Kantha et al.* [1986] on a 30-level, $\frac{1}{4}° \times \frac{1}{4}°$ grid and then interpolated to the model grid. Figure 2 depicts the climatological temperature and salinity at the surface and at 500 m. The model is then run for 10 days diagnostically (temperatures and salinities held constant) and then prognostically for 30 days. During this time the Gulf Stream narrows; after the 30 days, there are incipient meanders and eddy formation.

3. MODEL CLIMATOLOGY AND OTHER STATISTICS

After the initial adjustment of 40 days the model was run for 1 year. After the year and some months the separation point abruptly moves north of Cape Hatteras and the calculations are no longer considered usable in the absence of data assimilation. (Recent experiments with higher vertical resolution and with surface heat flux included show significant improvement, maintaining realistic Gulf Stream separation for at least 5 years.) Synoptic model realizations will be discussed later in connection with assimilation results. The model "climatology" is therefore represented by year-long averages archived at 5-day intervals; henceforth, these climatological variables are denoted by angle brackets. Figure 3 shows the climatological temperature and salinity at the surface, $\langle T \rangle(x, y, 0)$ and $\langle S \rangle(x, y, 0)$, and at 500 m; they may be compared to the observed climatology in Figure 2. The agreement between the model climatology and the observed climatology is generally good. There are differences. First, there are somewhat larger surface temperatures in the model climatology than in the observed climatology; including realistic surface heat flux should improve the model climatology. Second, there are large surface salinity gradients in the observed climatology (at 31°N and 37°N,
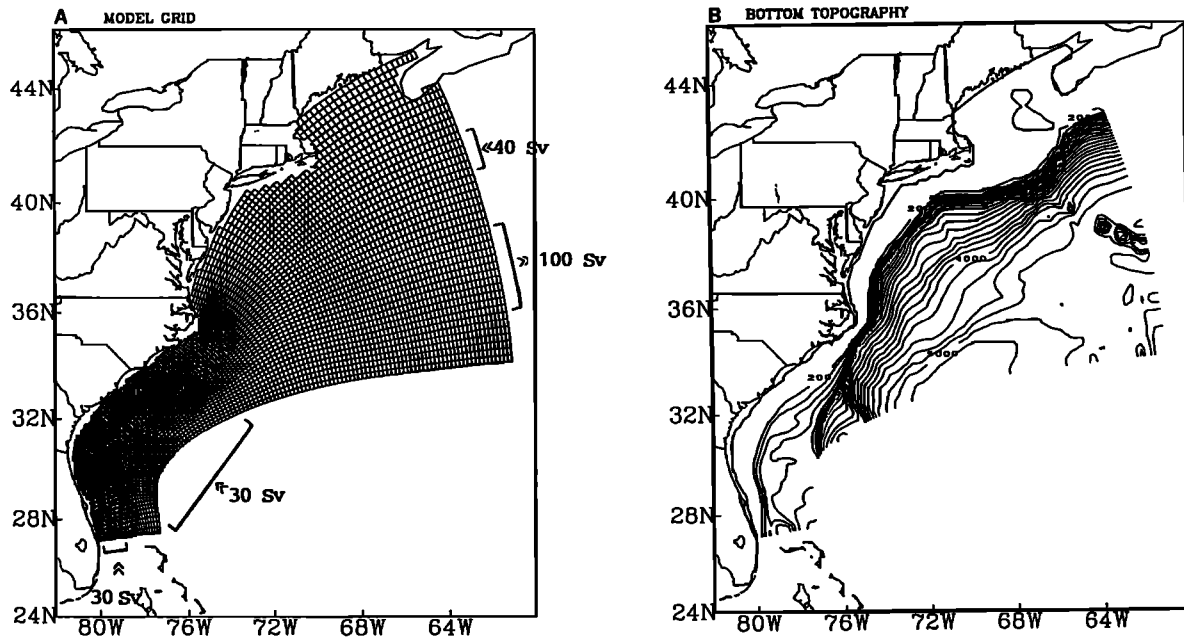
Fig. 1. (a) The curvilinear orthogonal model grid, where nonzero, total transport inflow/outflow boundary conditions are indicated. (b) The bottom topography of the model. The contour interval is 200 m and the heavy contour is the land boundary of the model at 20 m depth.

Figure 2) which are absent in the model climatology (Figure 3); this discrepancy is due to the lack of freshwater inflow in the present model.

The climatological elevation $\langle\eta\rangle(x, y)$ and total stream function $\langle\Psi\rangle(x, y)$ are shown in Figure 4. Note the development of the northern recirculation gyre [Hogg et al., 1986] in the stream function and the permanent meander at 69°W in the surface elevation. The latter is often seen in IR SST maps
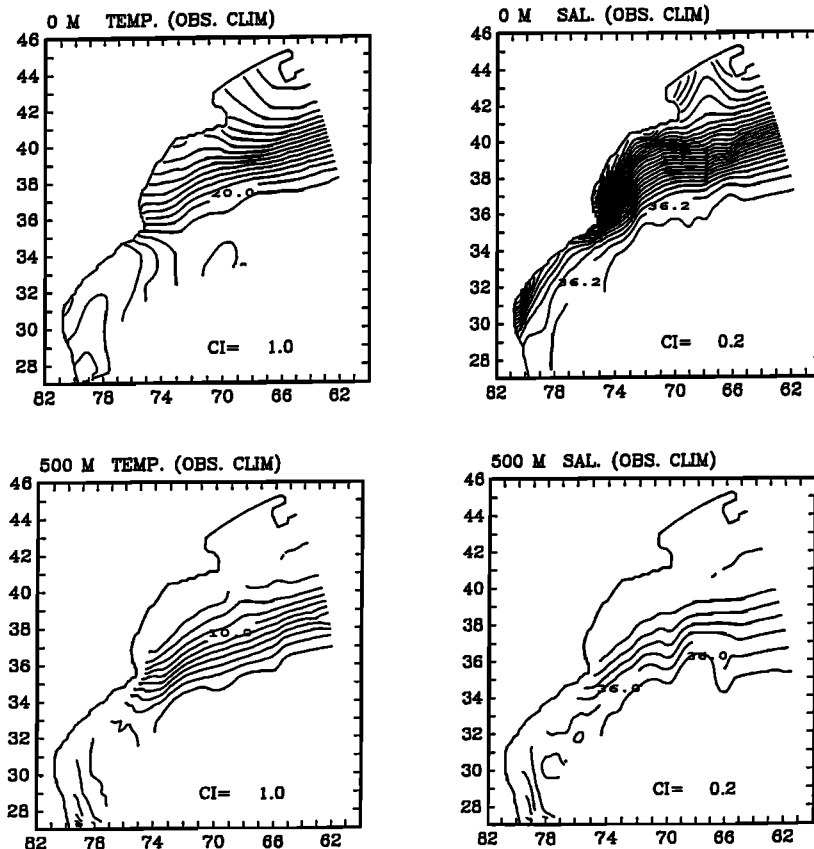
Fig. 2. The observed climatology used to initialize the model. (Left) The temperature and (right) the salinity at (top) the surface and (bottom) 500 m are shown. The contour intervals are 1°C for temperature and 0.2 ppt for salinity.
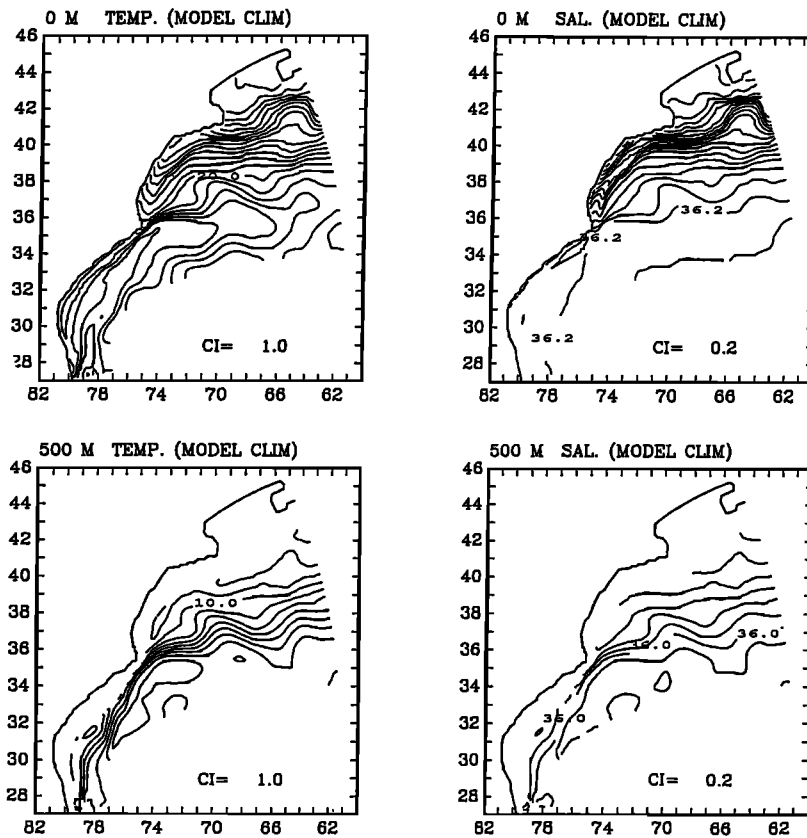
Fig. 3.   Same as Figure 2, but for the model climatology (i.e., 360-day average).

of the Gulf Stream (P. Cornillon, personal communication, 1990). Figure 5 shows velocity fields at the surface and at a depth of 2000 m; we select the latter to show the western boundary undercurrent developed by the model. The undercurrent is the deepwater continuation of the (40 Sv) flow imposed on the northeastern open boundary; the surface portion of this flow is entrained into the Gulf Stream. According to *Thompson and Schmitz* [1989] the undercurrent may be an important factor in the separation of the Gulf Stream.

The rms surface elevation anomaly and the eddy kinetic energy at the surface are shown in Figure 6. The maximum

values of the rms elevation anomaly and the surface eddy kinetic energy ($\sim$0.4 m and $\sim$0.3 m^2 s^{-2}, respectively) agree very well with observations [e.g., *Richardson*, 1983; *Shum et al.*, 1990; *Willebrand et al.*, 1990]. Note the rms elevation maxima at 73°W and at 79°W. The latter is located near the so-called "Charleston Bump" along the Florida shelf.

Since the model is a coastal ocean model as well as an eddy-resolving open ocean model, it can be used to study the interaction between the variability of the Gulf Stream and that of the coastal region [*Bane et al.*, 1988]. Thus Figure 7 shows the area-averaged rms elevation anomaly for different regions of the model. Generally, in deeper regions closer to
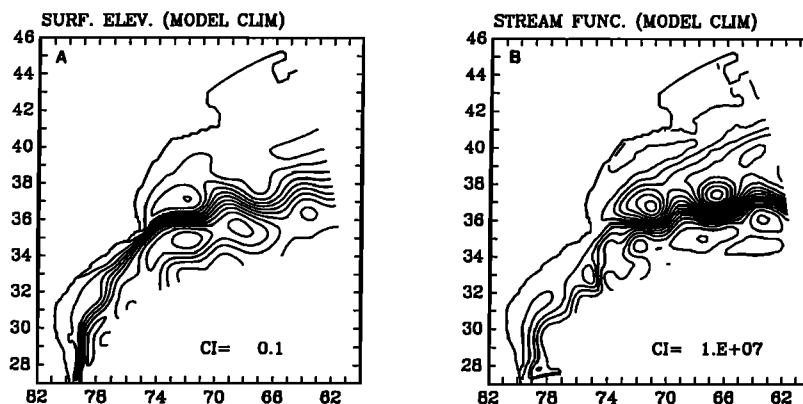
Fig. 4.   (a) The model climatology of surface elevation and (b) the total stream function. The contour intervals are 0.1 m and 10^7 m^2 s^{-1}, respectively.
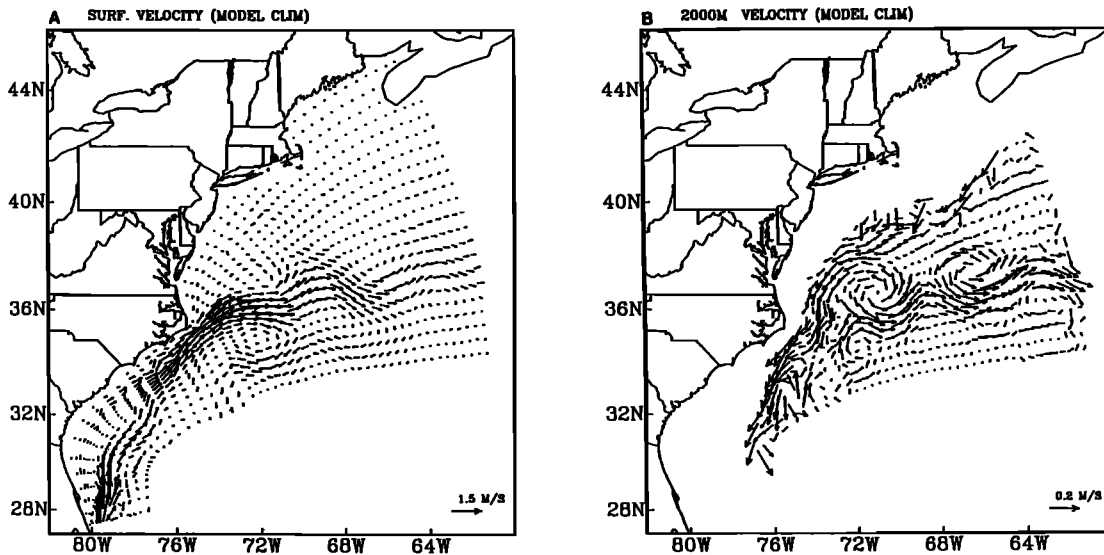
Fig. 5. (a) The model climatology of surface velocity and (b) the 2000-m velocity.

the Gulf Stream, larger variability is found. However, there are some events, such as day 90, that appear to affect all regions except the shelf simultaneously. These events are associated with periods of energetic meandering and warm core eddy formations. The main goal here, however, is to demonstrate the assimilation scheme described below, and we refer this discussion to future studies with an extended model domain and improved resolution.

Knowledge of the time and length scales associated with the variability of the Gulf Stream is useful to a priori estimates of predictability time scales and is needed in the optimal interpolation scheme discussed below. Therefore the autocorrelations of the surface elevation have been calculated at every grid point in the cross-stream and in the along-stream direction. The differences between the average along-stream and the average cross-stream length scales are only about 15 km so that the spatial autocorrelations are calculated as the average of the autocorrelations in the four directions. For each of the grid points an e-folding time and length scale is found. The area-averaged time scale over the whole region is 22 days with a standard deviation of 9 days

while the average length scale is 170 km with a standard deviation of 70 km. These scales are comparable to those found by Auer [1987]. The time and space scales vary significantly along the Florida Shelf, while smaller variations are found in the extension region of the Gulf Stream. In this paper we neglect these variations and use only the average length scales $k_x^{-1} = k_y^{-1} = 170$ km and time scale $k_t^{-1} = 22$ days (see (A15b)).

4. SUBSURFACE TO SURFACE CORRELATIONS

We define the correlation factors,

$$F \equiv \frac{\langle \delta \rho \, \delta \eta \rangle}{\langle \delta \eta^2 \rangle} \quad (6a)$$

$$F_T \equiv \frac{\langle \delta T \, \delta \eta \rangle}{\langle \delta \eta^2 \rangle} \quad (6b)$$

$$F_S \equiv \frac{\langle \delta S \, \delta \eta \rangle}{\langle \delta \eta^2 \rangle} \quad (6c)$$
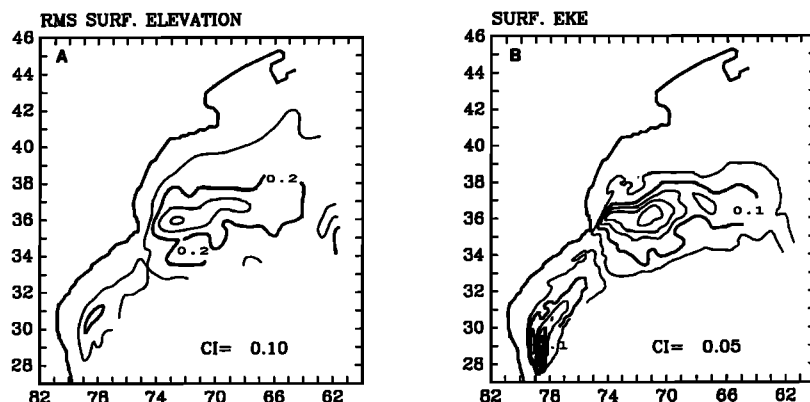
Fig. 6. (a) The rms surface elevation anomaly and (b) the surface eddy kinetic energy, both of which are from the 1-year model calculation. The contour intervals are 0.1 m and 0.05 m^2 s^{-2}, respectively.

RMS SURFACE ELEVATION ANOMALY
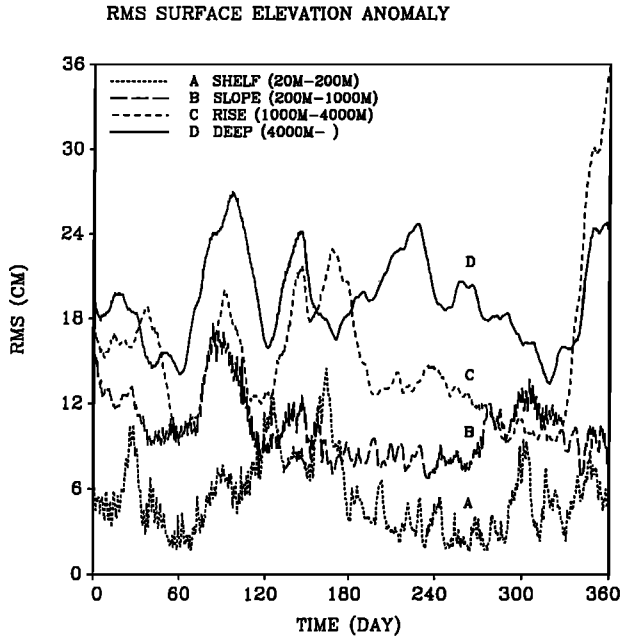
Fig. 7. The rms elevation anomaly for different regions of the model: the continental shelf (20–200 m) (curve A), the continental slope (200–1000 m) (curve B), the continental rise (1000–4000 m) (curve C), the deep ocean ($H > 4000$ m) (curve D).

and the correlation coefficients,

$$C \equiv \frac{\langle \delta\rho \; \delta\eta \rangle}{[\langle \delta\rho^2 \rangle\langle \delta\eta^2 \rangle]^{1/2}} \qquad (7a)$$

$$C_T \equiv \frac{\langle \delta T \; \delta\eta \rangle}{[\langle \delta T^2 \rangle\langle \delta\eta^2 \rangle]^{1/2}} \qquad (7b)$$

$$C_S \equiv \frac{\langle \delta S \; \delta\eta \rangle}{[\langle \delta S^2 \rangle\langle \delta\eta^2 \rangle]^{1/2}} \qquad (7c)$$

where $\delta\eta = \eta - \langle\eta\rangle$, $\delta\rho = \rho - \langle\rho\rangle$, etc.

The correlation coefficient C is plotted in Figure 8. Large portions of the domain exceed values of 0.8, particularly in the extension region of the Gulf Stream; values are lower in shallow water and near the open boundaries. There are relatively small vertical variations in the upper 1000 m. Note that if $|C| = |C_T| = |C_S| = 1$, then

$$\delta\rho(x, y, z, t) = F(x, y, z) \; \delta\eta(x, y, t) \qquad (8a)$$

$$\delta T(x, y, z, t) = F_T(x, y, z) \; \delta\eta(x, y, t) \qquad (8b)$$

$$\delta S(x, y, z, t) = F_s(x, y, z) \; \delta\eta(x, y, t) \qquad (8c)$$

exactly. Equation (8a) is, of course, suggested by the hydrostatic relation; in deep water, if the horizontal gradients of the pressure anomaly are small below some depth H_0, then $\rho_0^{-1} \int_{H_0}^{0} F \, dz = -1$.

Now the relation between density, temperature, and salinity in the model is constrained by the equation of state and by the inherent model T-S correlation such that $\delta T \simeq T_\rho \, \delta\rho$ and $\delta S \simeq S_\rho \, \delta\rho$ where T_ρ and S_ρ are derivatives of T and S with respect to ρ. If one assumes that these relations are exact, then one finds that

$$|C_T| = |C_S| = |C| \qquad (9)$$
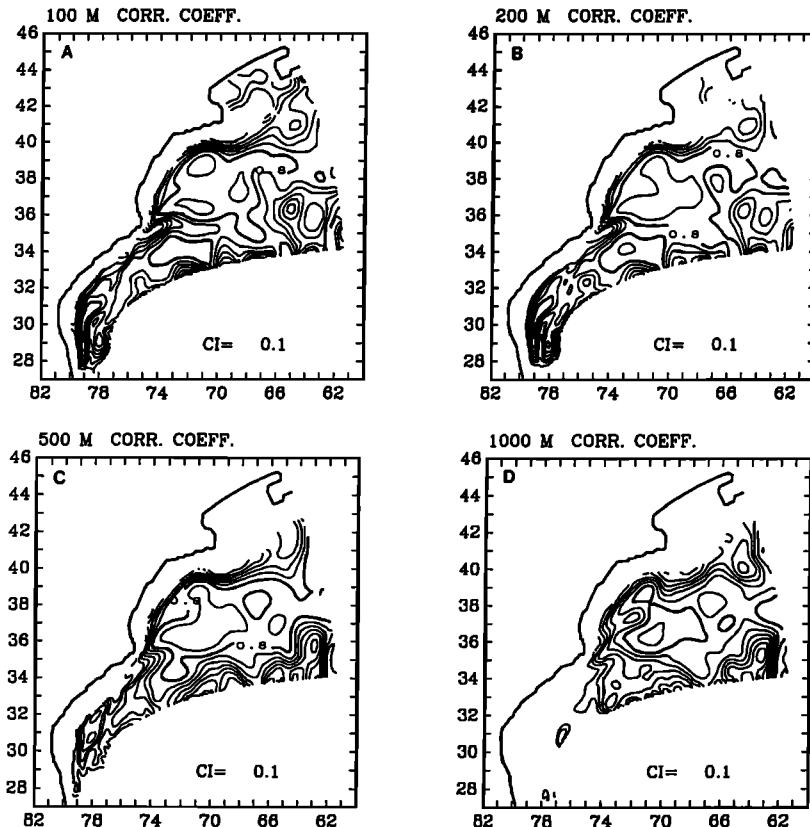
Fig. 8. The correlation coefficient C of (7) at (a) 100 m, (b) 200 m, (c) 500 m, and (d) 1000 m. The $C = 0.8$ contour is highlighted.
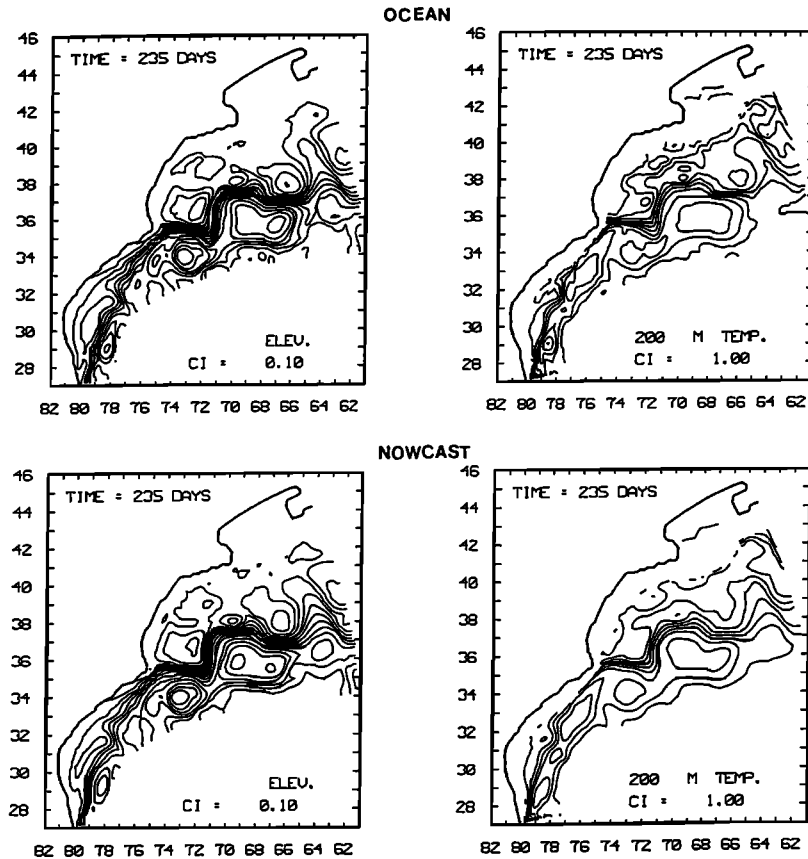
Fig. 9. (Left) The surface elevation and (right) the temperature at 200 m on day 235 of the year-long run (day 15 of the control ocean). (Top) The control ocean and (bottom) the nowcast, i.e., the diagnostic adjustment of the elevation to the temperature and salinity fields obtained by (10), are shown. The area-averaged rms error for surface elevation is 0.04 m.

which is a simplification used in Appendix A. Actual evaluation of $(7a)$–$(7c)$ using model results shows that (9) is a very good approximation except near singular surfaces in x-y-z space where $S_p = 0$; however, there $F_S = 0$.

5. A TEST OF THE SURFACE TO SUBSURFACE CORRELATION TECHNIQUE

We first test the subsurface correlation technique alone. Thus we choose day 235 of the model itself since it significantly departs from the climatology. (As defined in the next section, this day is also day 15 of the control ocean.) We extract only the elevation anomaly $\delta\eta$ at every model grid point.

The analysis temperature T_A and salinity S_A are then obtained according to

$$T_A = \langle T \rangle + F_T \, \delta\eta \qquad (10a)$$

$$S_A = \langle S \rangle + F_S \, \delta\eta \qquad (10b)$$

The model is then run diagnostically (temperature, salinity, and density are held constant) for 10 days to obtain dynamically (nearly geostrophically) adjusted velocity fields and, by the way, a new elevation field. The associated elevation anomaly field will differ from $\delta\eta$ at day 235 from the model year run because of error in the assumption that $F(x, y, z)$ is invariant in time, numerical errors, and the fact that tendency terms are null in the 10-day diagnostic run.

The elevation fields and 200-m temperature fields for day 235 are compared to the corresponding nowcast fields in Figure 9. The global (area averaged) rms error between the control elevation and the nowcast elevation is about 0.04 m (0.05 m excluding the shelf) or 15% error compared with the rms error of the unassimilated ocean on that day (see section 8 and Figure 14). As discussed in sections 7 and 8, the global rms error of an assimilation where data are only available on satellite tracks is about 2–3 times larger. This indicates that the error associated with imperfect altimetry coverage is larger than the error associated with imperfect surface to subsurface correlations.

A 15-day forecast is compared with day 250 in Figure 10. Note that the forecast predicts the development of a warm intrusion at 70°W, 38°N. In the forecast, however, the intrusion separated from the Gulf Stream a few days before the control ocean (not shown). The rms elevation error, the difference between the forecast and the control ocean, increases now to 0.12 m (0.14 m excluding the shelf) or 43% of the error of the unassimilated model.

6. THE NOWCAST/FORECAST SYSTEM

Surrogate satellite altimetry data which conform to the Geosat Exact Repeat Mission (ERM) coverage is extracted from the year-long model calculation of surface elevation.

The track location and schedule of the simulated Geosat tracks are shown in Figure 11 and listed in Table 1. In this paper we define the tracks by the nearest model grid points.
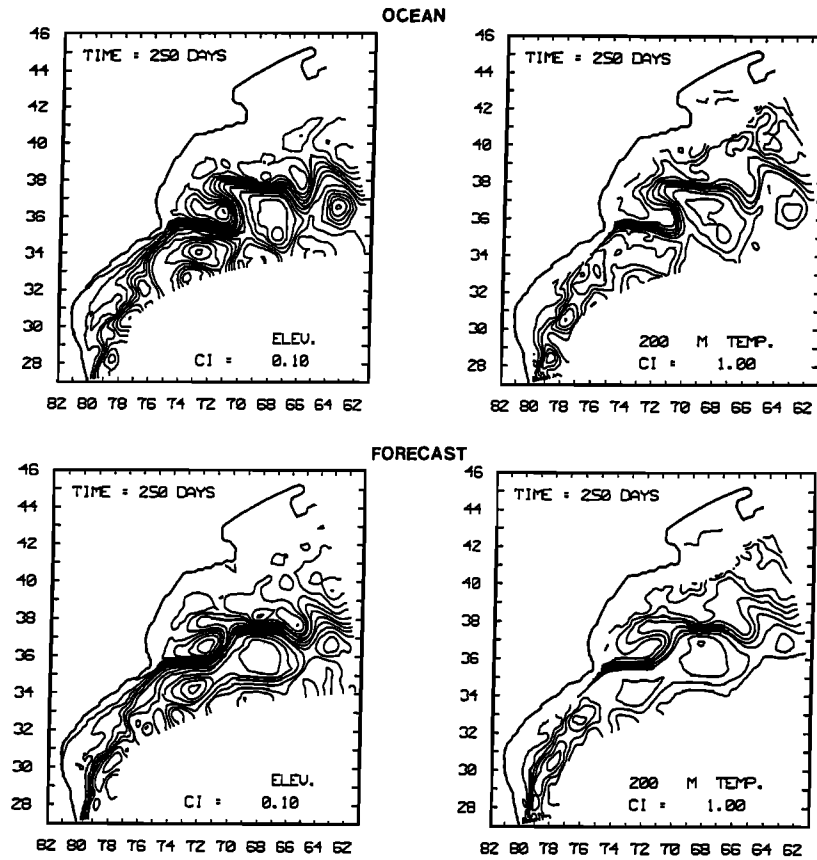
Fig. 10. As in Figure 7 but for day 250 of the year-long run (day 30 of the control ocean). Thus the bottom panels are the 15-day forecast. The area-averaged rms error for surface elevation is 0.12 m.
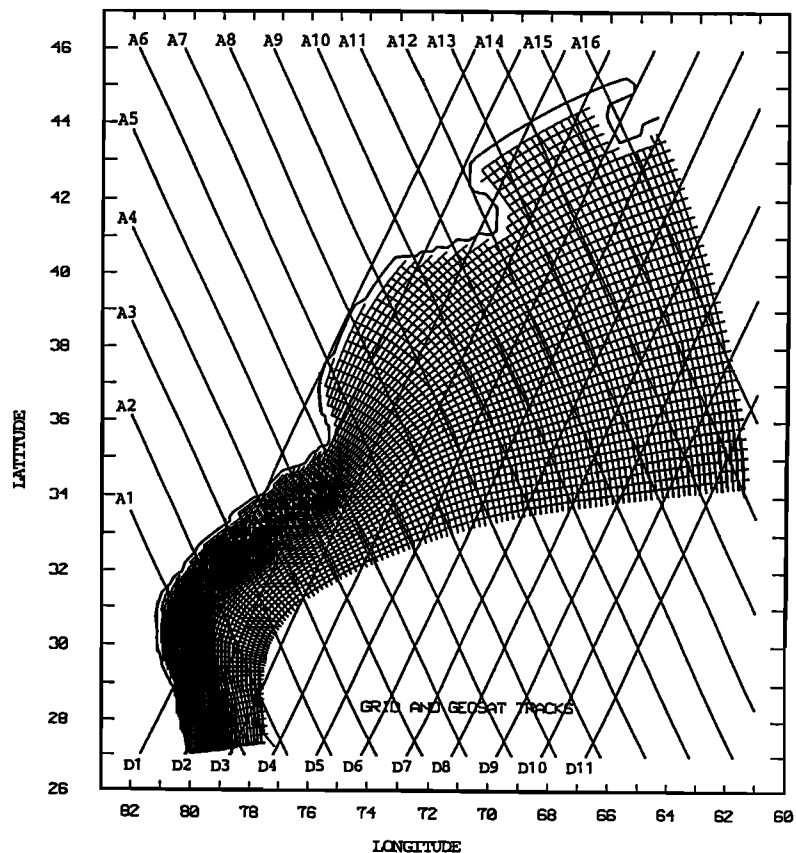
Fig. 11. The model grid and the Geosat tracks used in the assimilation. A1 through A16 and D1 through D11 are the ascending and descending tracks, respectively.

TABLE 1. Sampling Schedule of the Geosat ERM Over the Modeled Area

	Day																
	1	2	3	4	5	6	7	8	9	10	11	12	13	14	15	16	17
							Ascending Tracks										
Track number	1	7	13	2	8	14	3	9	15	4	10	16	5	11	6	12	
Number of data points	23	25	44	25	31	46	17	36	46	16	39	38	17	42	21	46	0
							Descending Tracks										
Track number	1	7	...	2	8	...	3	9	...	4	10	...	5	11	6	...	
Number of data points	47	48	0	76	37	0	82	29	0	63	23	0	62	10	55	0	0

The track numbers refer to Figure 11. Ascending tracks are at the beginning of each day, while the descending tracks are at the middle of each day. The distance between data points along each track is taken to be 25 km. This schedule is repeated every 17 days and includes 1044 data points. The number of model grid points is 5445.

For the area considered here, there are 16 ascending tracks and 11 descending tracks, such that there are either one, two, or no tracks per day; there are an average of only 60 data points per day which may be compared to the 5445 horizontal grid points of the model. Each track is repeated every 17 days. The data points along each track are equally spaced and are sampled simultaneously. (The time for a satellite to traverse the region is very small compared to the elevation anomaly decorrelation time.) The track spacing at mid-latitudes is about 140 km, and the spacing of data along tracks is about 7 km. For this study we have subsampled the model data at intervals of 25 km. Note again that the spatial decorrelation scale is about 170 km (see section 3). *White et al.* [1990a, b] show that since the track separation scale dominates, little is gained by smaller along-track spacing. With this realistic but limited coverage we try to find the best assimilation scheme.

The complete nowcast/forecast cycle is shown in Figure 12. If we break into the cycle after the point labeled "reset time level," we begin with a model forecast at time level n. In the box labeled "Data Assimilation" a standard optimal interpolation technique is used so that analysis fields for the surface elevation and subsurface temperature and salinity are obtained according to

Fig. 12. The altimetry nowcast/forecast scheme. A suggested starting point of the cycle is immediately after "reset time level."

$$\eta_{Ai} = \eta_{Mi} + \sum_\alpha^N P_{i\alpha}^\eta [\delta\eta_{0\alpha} - \delta\eta_{M\alpha}] \qquad (11a)$$

$$T_{Ai} = T_{Mi} + \sum_\alpha^N P_{i\alpha}^T [\langle T_\alpha\rangle + F_{T\alpha}\delta\eta_{0\alpha} - T_{M\alpha}] \qquad (11b)$$

$$S_{Ai} = S_{Mi} + \sum_\alpha^N P_{i\alpha}^S [\langle S_\alpha\rangle + F_{S\alpha}\delta\eta_{0\alpha} - S_{M\alpha}] \qquad (11c)$$

where we have directly inserted the "observations" $T_{0\alpha} = \langle T_\alpha\rangle + F_{T\alpha} \delta\eta_{0\alpha}$ and $S_{0\alpha} = \langle S_\alpha\rangle + F_{S\alpha} \delta\eta_{0\alpha}$ according to (8b) and (8c). The quantities with the subscript M are the model prognostic fields or the first-guess fields. The quantities with the subscript A are the analysis fields and the initial conditions for the next prognostic calculation. Roman subscripts represent the model grid point locations at the analysis time. Greek subscripts denote the satellite locations and time.

The weights $P_{i\alpha}$ are determined by an optimal interpolation method, described in detail in Appendix A; the method makes use of anomaly covariance matrices determined from the year-long, "climatological" model run. The weighting factors for model grid points near a new satellite track are relatively large while those spatially and temporally distant from the track are relatively small. The weights are reduced to account for the errors in (8a)–(8c) associated with correlations less than unity; these errors are detailed in Appendix B.

After assimilation of the elevation temperature and salin-

TABLE 2. Error Sensitivity to the Parameters Δt^a and N

	Δt^a, days			
N	0.5	1	3	6
2	43.9	44.0	45.9	47.7
6	42.3	42.7	45.1	47.3
12	42.3	42.7	44.3	46.4

Δt^a is the time between data assimilations, and N is the number of "observational" data points used to update each grid point. The values are area-averaged rms error of the assimilated elevation field compared with the unassimilated rms error (24.6 cm) all averaged over a 30-day period; the results are expressed in percentiles.

ity anomalies, the velocity field from the previous prognostic run will not be in geostrophic equilibrium with the new density and elevation fields. The model could be run diagnostically as was done in section 4. However, good results are obtained more economically by a calculation represented by the box labeled "Geostrophic Adjustment" in Figure 12. It is a geostrophic calculation for the difference (analysis minus first guess) velocity field due to the difference density and elevation fields.

The observational data to be assimilated into a single model grid point are the N points having the least error covariance relative to the model grid point (see Appendix A).

In the future the elevation anomaly will be obtained from satellite data, in which case $\delta\eta_0$ will be the observed sea surface height relative to the observed satellite climatology; thus the geoid problem is avoided. In this paper we use the "identical twin" approach whereby data is subsampled from the model itself to supply surrogate data. The "observed" elevation climatology and the model climatology are identical.

The model runs discussed in the paper are as follows. (1) The "true ocean" or control ocean from which we obtain the surrogate altimetry data begins on day 220 of the year-long run. (2) The unassimilated model run was initialized with day 40 of the year-long run. (3) The assimilated model run was also initialized with day 40 of the year-long run while data sampled from run 1 are assimilated. The rms error of the unassimilated run is defined as the (area averaged) rms difference between the fields (e.g., surface elevation) calculated by run 2 and the fields calculated by run 1, while the

rms error of the assimilated run is defined as the rms difference between run 3 and run 1. Runs 2 and 3 are independent of run 1 since their initial conditions are separated by an interval of time that is much longer than the decorrelation time scale of this region.

7. EVALUATION OF THE OPTIMAL INTERPOLATION SCHEME

Before attempting dynamical assimilation into the prognostic model, we first wish to assay the sensitivity of the data assimilation scheme, by itself, to the assimilation parameters such as the time interval between assimilations, Δt^a, and the number of "observational" data points, N, that are used to correct one grid point. Thus in Figure 12 we bypass the blocks labeled "Geostrophic Adjustment" and "Model Prognostic Run" such that $T_M^{n+1} = T_A^n$, etc. There are no velocities. Here, and in the following sections, we refer to this continuous optimal interpolation process as "statistical assimilation" to distinguish it from "dynamical assimilation" where the model dynamics participate in the process.

We calculate the area-averaged rms error between the assimilated model and the control ocean and also the rms error between the unassimilated model and the control ocean. The rms error of the assimilated model is normalized by the rms error of the unassimilated ocean, and the result is expressed in percentiles. Thus a 100% error means that the assimilated model gives an estimate of the control ocean that is no better than the unassimilated ocean, while a 0% error means that the assimilated model is identical to the control ocean. To make things simple, we will cite here only elevation data. Assimilation of subsurface fields (e.g., temperature) is discussed in the next section.

The time interval between assimilative updating of the model, Δt^a, can be equal to or larger than the time between observations; for the Geosat ERM it is 0.5 day or longer. For a larger assimilation time step the data of several tracks are saved. The number of observations, N, used to update a single model grid point can be one or more. The data points selected for each grid point are the ones with the best correlation in space and time.

We do not find that there is great sensitivity to the choice of Δt^a and N, and this is illustrated in Table 2. For example,

TABLE 4. The Effect of C_{FG} (see section 8) on the Dynamic Interpolation

	Region				
	Shelf	Slope	Rise	Deep Ocean	All Regions
Depth, m	0–200	200–1000	1000–4000	4000 and up	
Area percentile	19.5	13.2	21.8	45.5	100
Unassimilated rms error, cm	6.6	18.2	19.7	32.0	24.6
Error percentile					
$C_{FG}^2 = 0.1$	93.9	48.3	65.5	58.7	59.3
$C_{FG}^2 = 0.5$	109.1	41.2	46.2	43.7	45.5
$C_{FG}^2 = 1.0$	131.8	39.6	43.6	40.3	45.9
$C_2 = 1.0$	198.5	46.2	45.2	40.3	47.6

The tabulated percentiles are the regional rms error of the assimilated elevation field normalized with the unassimilated rms error, averaged over a 30-day period. These experiments were done with $\Delta t^a = 1$ day and $N = 6$. Note that if $C = 1$, the weights are independent of depth and are independent of C_{FG}.
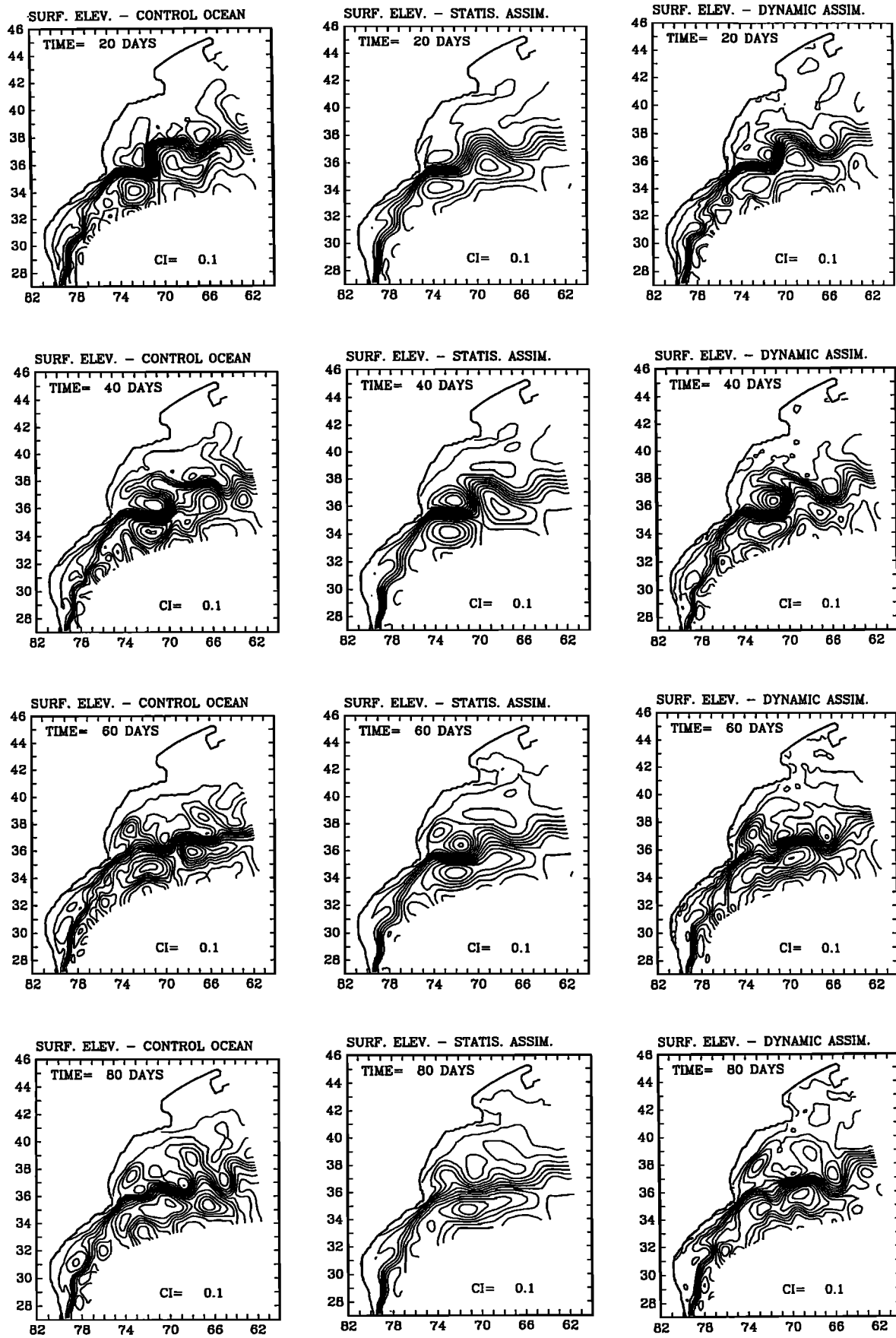
Fig. 13. The surface elevation on days 20, 40, 60, and 80: (left) the control ocean, (center) the statistically assimilated ocean, and (right) the dynamically assimilated ocean.

RMS ERROR – SURF. ELEVATION
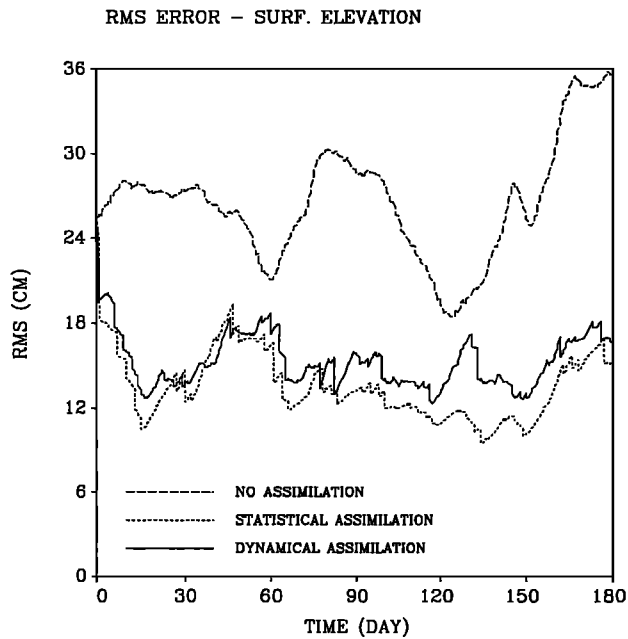
Fig. 14. A comparison between the area-averaged (excluding the shelf) rms error of surface elevation calculated by the dynamical assimilation (solid curve) and the one calculated by the statistical assimilation (short-dashed curve). The rms error of the unassimilated model is also shown (long-dashed curve).

either Δt^a = 0.5 day or Δt^a = 1.0 day is sufficiently small relative to the decorrelation time scale. Using $N > 6$ data points simply adds points which are quite distant from a model grid point relative to the spatial decorrelation distance. With the current track spacing, it seems that 42% error is about the best that the statistical assimilation can do. Note that the computer time needed for the assimilation scheme increases with decreasing Δt^a and increasing N; Table 3 summarizes this information.

We note that *White et al.* [1990*a*, *b*, *c*] assimilated data at every time step. This required up to 5 times more computations than with no assimilation, whereas the present scheme increases the computation time by only about 10%.

8. DYNAMICAL INTERPOLATION NOWCASTING AND FORECASTING

We now restore the role of the prognostic model in providing a first guess to the optimal interpolation scheme as diagramed in Figure 12. A prognostic model calculation provides the first-guess fields for the next assimilation. The weighting factors $P_{i\alpha}$ in (11*a*)–(11*c*) depend on the correlation between the elevation and the subsurface fields, C, and on the parameter C_{FG}, which relates the first-guess error covariance to the anomaly covariance (equal to one half the error covariance between two independent model runs). In Appendix A it is shown that the weights used to update temperature and salinity depend on the factor $C_{FG}^2/(1 + C_{FG}^2 - C^2)$. In regions where the correlation is poor, more weight is given to the model with respect to the weight given to the surrogate observational data. The results of sensitivity tests of the effect of C_{FG} are shown in Table 4. In the shallow area of the continental shelf the effects of this parameter are most pronounced. In this part of the model the variability is relatively small (unassimilated rms error of only

6.6 cm), but noise is produced by the updating procedure. This noise is reduced with small values of C_{FG} since the correlation coefficient C is small there too. In the other regions the rms error is not very sensitive to C_{FG}^2, though values greater than 0.5 are suggested. Note that if we assume that C = 1, the weights are independent of depth (and independent of C_{FG}). This case is slightly worse than the depth dependent cases.

Our results suggest that reduced errors may be obtained with a spatially varying C_{FG}. However, in this paper the parameters for dynamical interpolation using the prognostic model will be set at C_{FG} = 0.5, Δt^a = 1 day, and N = 6.

Figure 13 shows a sampling of synoptic realizations of the surface elevation of control ocean, statistical assimilation, and dynamical assimilation runs. It would appear that dynamical assimilation represents the control ocean better than statistical assimilation does. For example, notice the wide meander at 68°W on day 20, which narrows on day 40, creating a warm core eddy that interacts with the Gulf Stream at 72°W on day 60; later, a new eddy starts to form at 68°W on day 80. The statistically assimilated elevation fields show less variability, smaller spatial gradients, and reduced eddy energetics. However, if we compare the rms errors in Figure 14 (and include the error of the unassimilated run for later discussion), the error of the statistical assimilation is a bit less than that of the dynamical assimilation. This is puzzling but is partially explained by the fact, as seen in Figure 15, that the rms variability of the elevation anomaly of the statistical assimilation is significantly lower than that of the dynamical assimilation, whereas the latter is comparable to that of the control ocean. In other words, the model dynamics reinstate most of the variability lost by the filtering effect of the optimal interpolation process and the course Geosat sampling tracks. From Figure 13 this would seem to be a positive attribute, but the additional variability together

RMS ANOMALY – SURF. ELEVATION
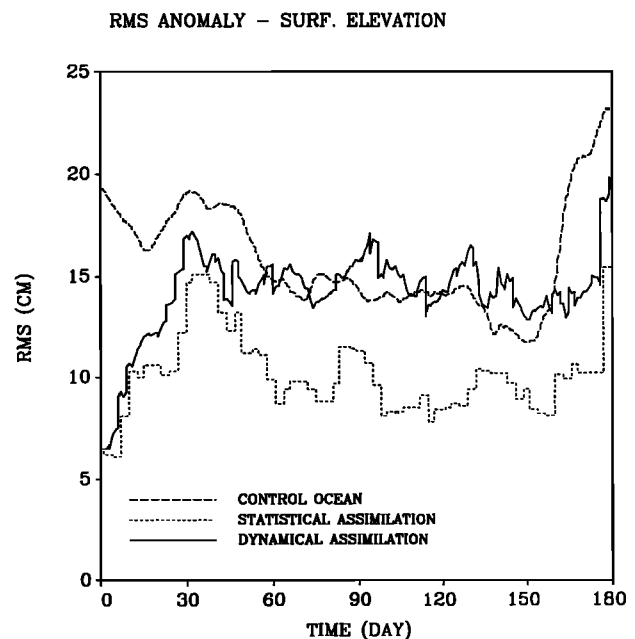
Fig. 15. Area-averaged (excludind the shelf) rms elevation anomaly of the control ocean (long-dashed curve) compared with the statistically assimilated ocean (short-dashed curve) and the dynamically assimilated ocean (solid curve).

RMS ERROR — 200M TEMP.

RMS ERROR — 500M TEMP.

RMS ERROR — 1000M TEMP.

RMS ERROR — 1500M TEMP.
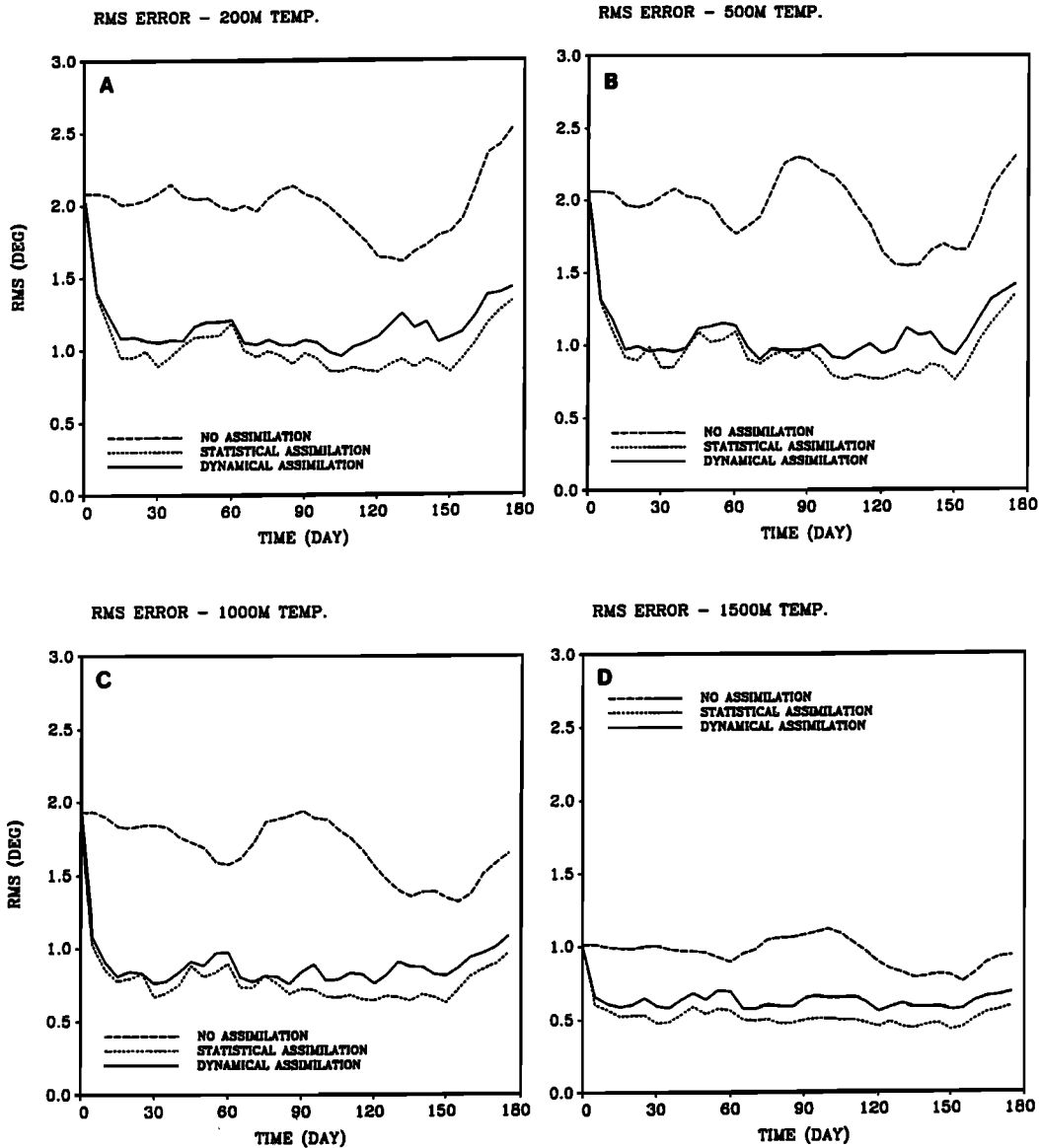
Fig. 16. Same as Figure 14 but for the rms error of temperature at (a) 200 m, (b) 500 m, (c) 1000 m, and (d) 1500 m.

A. FORECAST STARTS ON DAY 15

B. FORECAST STARTS ON DAY 35
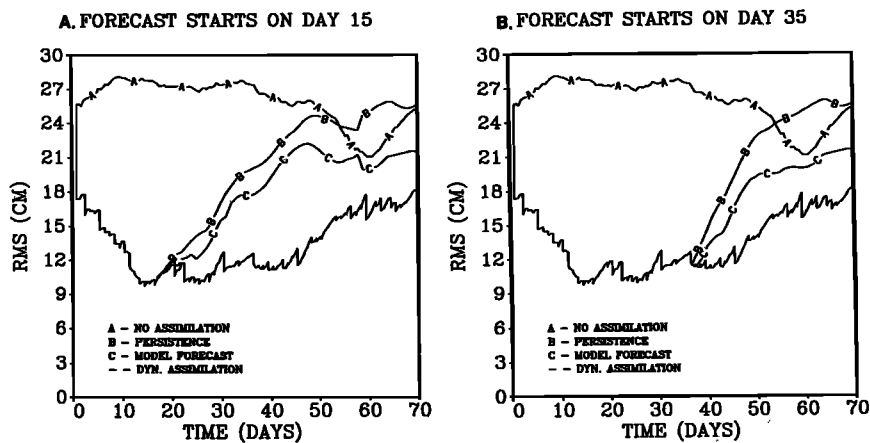
Fig. 17. The global rms error of the nowcast and the forecast experiments: (a) the forecast starts on day 15 and (b) the forecast starts on day 35. The unassimilated model, the persistence forecast, the model forecast, and the dynamical assimilation nowcast are indicated by curves A, B, and C and the solid curve, respectively.

with model phase errors evidently increases the rms error by a small amount. If, on the other hand, the dynamically assimilated fields are smoothed (filtered) so that the rms anomaly is comparable to that of the statistically assimilated fields (not shown), then the rms error of the former is lower than that of the latter. We note here that comparisons have also been made using the so-called pattern correlation, $\Phi = \langle xy \rangle / (\langle x^2 \rangle \langle y^2 \rangle)^{1/2}$ where x and y are anomalies; one might suppose that this would reduce the anomaly variances. However, comparisons of the Φ values as in Figure 14 (not shown) show slightly higher values of the statistical assimilation correlations relative to the dynamical assimilation; this is reversed if the latter is filtered. To good approximation, so long as $0.5 < \langle x^2 \rangle / \langle y^2 \rangle < 2.0$, the rms error $\langle (x - y)^2 \rangle = 2(\langle x^2 \rangle \langle y^2 \rangle)^{1/2}(1 - \Phi)$ and is related to the pattern correlation and the anomaly variance.

White et al. [1990a] provide a more detailed treatment of space scales. They obtained the not unexpected result that larger scales of the dynamically assimilated fields, relative to the satellite track spacing, compare better with those of the control run than do the smaller scales. Of course, dynamical assimilation automatically incurs error relative to statistical assimilation since, as discussed in section 5, the correlations between surface elevation and subsurface properties contain error. This error is, however, the cost of obtaining dynamically adjusted surface and subsurface, nowcast fields which are suitable initial conditions for forecasts.

We now focus on the errors of the dynamically assimilated fields versus errors of the unassimilated fields in Figures 14 and 16. The rms error of surface elevation, assimilated fields is about 40–45% of the unassimilated fields while the rms error of the subsurface temperature, assimilated fields is about 50–55% of the unassimilated fields. Together with the results of section 5 we conclude that the entire scheme is a feasible way of obtaining nowcasts.

We now examine the possibility of using the continuous, dynamically assimilated, nowcast fields as initial conditions for forecasts. Figures 17a and 17b show the result of nowcasts and forecasts where the forecasts begin at day 15 and day 35, respectively. Curves for model runs with no assimilation and with assimilation together with model forecasts are shown. We also show the forecasts using persistence. The model forecasts in these two experiments are better than the persistence forecast and the unassimilated runs; after 25–35 days the forecast is not significantly better than unassimilated runs. Note that the rate of error growth in the forecast is only slightly smaller than that of persistence at the beginning, but after about 20 days the error growth rate decreases. This could be associated with the fact that the initial forecast is dominated by short spatial scale variability that is not resolved by the Geosat data sampling scheme while, at a later time, "memory" of the larger-scale variability is retained. From the results of section 5 we surmise that denser altimetry data, for example, should improve the nowcast, reducing the area-averaged rms error by a factor of 2–3; consequently, the resultant forecast should also improve.

9. CONCLUSIONS AND DISCUSSION

The principle finding of this study is that continuous assimilation of elevation data in conjunction with predetermined correlations between elevation anomaly and subsur-

face temperature and salinity anomalies enables one to obtain nowcasts with errors of about 40–45% using Geosat track schedules. From results where complete areal coverage of elevation is available, we surmise that the a minimum error of about 15% is possible. From the two forecasts carried out here, it appears that starting from the nowcast, the forecast error approaches the unassimilated error after about 25 days.

We use a numerical model of the primitive equations with realistic bottom topography which includes the continental shelf and shelf break. The altimetry assimilation works best in deep water. Ultimately, the model should be driven with real winds, and satellite SST data should be incorporated as surface boundary conditions, in which case the coastal ocean would hopefully demonstrate nowcast and forecast skill (so long as wind forecasts retain skill). Of course, SST can be also used to position the Gulf Stream and associated eddies [*Robinson et al.* 1989; *Cornillon and Watts*, 1987] and should, in the future, be merged with the altimetry assimilation scheme.

There are other improvements that can be envisioned. There is, as always, a need for improved horizontal resolution, so that the Gulf Stream and mesoscale eddies are better represented numerically, and for improved vertical resolution, so that the surface and bottom mixed layer may be adequately reinstated in the model. In order to improve data assimilation and prognostic projection, it is apparent that the domain should be enlarged. We find that subsurface to surface correlations are degraded on the boundaries (Figure 8) and that the eddy variability is suppressed on the boundaries (Figure 6). On the other hand, if the focus is on the coastal ocean, the present domain might be judged adequate; in this case, additional computer resources can be invested, in improved nearshore resolution.

There are many possible alterations to the assimilation scheme. In fact, the limited success achieved here encourages further research and enhancement. The correlation factors might give way to empirical orthogonal functions obtained from the model or from real data; in fact, both should be obtained and compared. Subsurface information might be correlated with $\nabla^2(\delta\eta)$ (negative for cyclonic flow anomaly; positive for anticyclonic flow anomaly) in addition to $\delta\eta$ itself. Clearly, there is much to be done.

APPENDIX A: DESCRIPTION OF AN OPTIMAL INTERPOLATION METHOD

Standard Optimal Interpolation

We first review standard optimal interpolation (OI) methodology following closely the article by *Gustafsson* [1981]. We then specialize to our specific need to determine $P_{i\alpha}$ in (11a)–(11c).

Consider an observed property anomaly, f_α^0. It is the property value minus its climatological value; the subscript α denotes the spatial location and time of the observation. The "true" value of f at α is denoted simply as f_α with no superscript.

A first-guess anomaly f_i^f will be obtained as model output at a model grid point and at an analysis time, all denoted by the subscript i. Then, the first guess is corrected to obtain an analyzed value, f_i^a, according to

$$f_i^a = f_i^f + \sum_{\alpha}^{N} P_{i\alpha}(f_\alpha^0 - f_\alpha^f) \tag{A1}$$

Greek subscripts, in this case α, denote the observational grid point and observational time, and f_α^f is interpolated from model grid points and times to the observational point and time. For the present we neglect interpolation error. $P_{i\alpha}$ are the weights; the main job of OI is to determine these factors.

Errors are defined according to

$$f_i^f = \text{true anomaly} + \text{first-guess error} = f_i + f_i^f \tag{A2a}$$

$$f_i^0 = \text{true anomaly} + \text{observational error} = f_i + \Delta f_i \tag{A2b}$$

so that (A1) can be written

$$f_i^a = f_i + f_i^f + \sum_{\alpha}^{N} P_{i\alpha}(f_\alpha + \Delta f_\alpha - f_\alpha - f_\alpha^f) \tag{A3}$$

We next form the square of the analysis error; thus

$$E_i^a = \langle (f_i^a - f_i)^2 \rangle \tag{A4}$$

Now insert (A3) into (A4) and neglect cross correlations between the quantities Δf and f', so that

$$E_i^a = M_{ii} - 2 \sum_{\alpha}^{N} P_{i\alpha} M_{\alpha i} + \sum_{\alpha}^{N} \sum_{\beta}^{N} P_{i\alpha} P_{i\beta}[M_{\alpha\beta} + D_{\alpha\beta}] \tag{A5}$$

where we define

$$M_{\alpha\beta} = \langle (f_\alpha' f_\beta') \rangle \tag{A6a}$$

$$D_{\alpha\beta} = \langle \Delta f_\alpha \Delta f_\beta \rangle \tag{A6b}$$

$M_{\alpha\beta}$ is a space-time correlation of the first-guess error, and $D_{\alpha\beta}$ is the space correlation of the observational instrument error.

We now find the set of $P_{i\alpha}$ that minimizes E_i^a in (A5). Thus we successively set the partial derivatives $\partial E_i^a/\partial P_{i\lambda} = 0$ and note that $\partial P_{i\alpha}/\partial P_{i\lambda} = \delta_{\alpha\lambda}$ where $\delta_{\alpha\lambda}$ is the Kronecker delta function. The result is

$$\sum_{\alpha}^{N} P_{i\alpha}[M_{\alpha\beta} + D_{\alpha\beta}] = M_{i\beta} \qquad \beta = 1, \cdots, N \tag{A7}$$

Thus for every model grid point i one has to invert the matrix in (A7) to solve for $P_{i\alpha}$, which may subsequently be used in (A1).

The analysis error may be obtained by inserting (A7) into (A5) so that

$$E_i^a = M_{ii} - \sum_{\alpha}^{N} P_{i\alpha} M_{\alpha i} \tag{A8}$$

The magnitude of the first-guess error can be obtained as the analysis error plus the model error growth, $E_i^m \Delta t^a$. Thus

$$M_{ii}^{n+1} = E_i^{an} + E_i^m \Delta t^a \tag{A9}$$

where t^n is the assimilation time level and $\Delta t^a = t^{n+1} - t^n$ is the time between assimilations.

Present Application

As stated in section 3, we have found that $|C_T| \simeq |C_S| \simeq |C|$, and henceforth, we will approximate these relations as identities. Equation (8b) can be cast in the form of (A7) where, however,

$$M_{\alpha\beta} = \langle T_\alpha' T_\beta' \rangle \tag{A10a}$$

$$D_{\alpha\beta} = \langle \Delta T_\alpha \Delta T_\beta \rangle \tag{A10b}$$

We approximate the first-guess error according to

$$\langle T_\alpha' T_\beta' \rangle = F_T^2 \langle \delta\eta_\alpha' \ \delta\eta_\beta' \rangle + F_T^2 \left\{ \frac{1 - C^2}{C^2} \right\} \langle \delta\eta_\alpha' \ \delta\eta_\beta' \rangle \tag{A11}$$

where the second term on the right, to be derived in Appendix B, is the error due to the fact that the correlation between temperature and elevation is imperfect. Similarly,

$$\langle \Delta T_\alpha \Delta T_\beta \rangle = F_T^2 \langle \Delta\eta_\alpha \Delta\eta_\beta \rangle$$

$$+ F_T^2 \left\{ \frac{1 - C^2}{C^2} \right\} \langle \delta\eta_{0\alpha} \ \delta\eta_{0\beta} \rangle \tag{A12}$$

The second term in (A12) is an additive error of the "observation," $\langle T_\alpha \rangle + F_T \ \delta\eta_{0\alpha}$, due to the imperfect correlation.

We insert (A11) and (A12) into (A7) via (A10a) and (A10b) and neglect horizontal variations of F_T and C relative to the decorrelation scales discussed below. Then, after some rearrangement,

$$\sum_{\alpha}^{N} P_{i\alpha}^T [\langle \delta\eta_\alpha' \ \delta\eta_\beta' \rangle + (1 - C^2)\langle \delta\eta_{0\alpha} \ \delta\eta_{0\beta} \rangle$$

$$+ C^2 \langle \Delta\eta_\alpha \Delta\eta_\beta \rangle] = \langle \delta\eta_i' \ \delta\eta_\beta' \rangle \tag{A13}$$

For $C = 1$ the error due to imperfect correlation vanishes; the resulting equation is the analysis equation for elevation alone. For $C = 0$ the instrument error vanishes because zero correlation with temperature renders it irrelevant. We now set

$$\langle \delta\eta_{0\alpha} \ \delta\eta_{0\beta} \rangle = \langle \delta\eta_\alpha \ \delta\eta_\beta \rangle \tag{A14a}$$

$$\langle \delta\eta_\alpha' \ \delta\eta_\beta' \rangle = C_{FG}^2 \langle \delta\eta_\alpha \ \delta\eta_\beta \rangle \tag{A14b}$$

where $C_{FG} < 2$ is an unknown coefficient relating the first-guess error covariance with the climatological variability covariance. Instead of using (A9), we will search for the value of C_{FG} which yields the best nowcast.

A fairly conventional model of the covariances in (A13) and (A14) is

$$\langle \Delta\eta_\alpha \Delta\eta_\beta \rangle = D \ \delta_{\alpha\beta} \tag{A15a}$$

and

$$\langle \delta\eta_\alpha \ \delta\eta_\beta \rangle = \langle \delta\eta_\alpha^2 \rangle \exp \left[-(k_x \Delta x)^2 - (k_y \Delta y)^2 - (k_t \Delta t)^2 \right] \tag{A15b}$$

where $\Delta x = x_\alpha - x_\beta$, $\Delta y = y_\alpha - y_\beta$, and $\Delta t = t_\alpha - t_\beta$. All times are relative to the analysis time. To use the assimilation scheme, one must supply values for D, k_x, k_y, k_t, and C_{FG}.

If we insert (A14a), (A14b), and (A15a) into (A13), we obtain

$$\sum_{\alpha}^{N} P_{i\alpha}^{T}[(1 + C_{FG}^2 - C^2)\langle \delta\eta_\alpha \ \delta\eta_\beta\rangle + D \ \delta_{\alpha\beta}]$$

$$= C_{FG}^2\langle \delta\eta_i \ \delta\eta_\beta\rangle \qquad (A16)$$

For the identical twin experiments, $D = 0$. Thus it is possible to solve

$$\sum_{\alpha}^{N} P_{i\alpha}^{\eta}\langle \delta\eta_\alpha \ \delta\eta_\beta\rangle = \langle \delta\eta_i \ \delta\eta_\beta\rangle \qquad (A17)$$

and then

$$P_{i\alpha}^{T}(x, y, z) = \frac{C_{FG}^2}{1 + C_{FG}^2 - C^2(x, y, z)} P_{i\alpha}^{\eta}(x, y) \qquad (A18)$$

Furthermore, $P_{i\alpha}^{s} = P_{i\alpha}^{T}$.

APPENDIX B: THE SUBSURFACE CORRELATION ERROR

Instead of (8b), let $\delta T = F_T \ \delta\eta + \Delta_c T$ where $\Delta_c T$ is the correlation error so that

$$C_T = \left[\frac{\langle \delta T \ \delta\eta\rangle}{\langle \delta T^2\rangle\langle \delta\eta^2\rangle}\right]^{1/2} = \frac{F_T\langle \delta\eta^2\rangle}{[F_T^2\langle \delta\eta^2\rangle + \langle \Delta_c T^2\rangle]^{1/2}[\langle \delta\eta^2\rangle]^{1/2}}$$

$$(B1)$$

since the correlation between $\Delta_c T$ and $\delta\eta$ are, by definition, null. The above equation may be written

$$\langle \Delta_c T^2\rangle = F_T^2 \frac{1 - C_T^2}{C_T^2} \langle \delta\eta^2\rangle \qquad (B2)$$

and is the error due to imperfect correlation, $C_T^2 < 1$.

REFERENCES

Auer, S. J., Five-year climatological survey of the Gulf Stream system and its associated rings, *J. Geophys. Res.*, *92*, 11,709–11,726, 1987.

Bane, J. M., O. B. Brown, R. H. Evans, and P. Hamilton, Gulf Stream remote forcing of shelfbreak currents in the Mid-Atlantic Bight, *Geophys. Res. Lett.*, *15*, 405–407, 1988.

Berry, P., and J. Marshall, Ocean modeling studies in support of altimetry, *Dyn. Atmos. Oceans*, *13*, 269–300, 1989.

Blumberg, A. F., and G. L. Mellor, Diagnostic and prognostic numerical circulation studies of the South Atlantic Bight, *J. Geophys. Res.*, *88*, 4579–4592, 1983.

Blumberg, A. F., and G. L. Mellor, A description of a three-dimensional coastal ocean circulation model, in *Three-Dimensional Coastal Ocean Models*, *Coastal Estuarine Sci.*, vol. 4, edited by N. S. Heaps, pp. 1–16, AGU, Washington, D. C., 1987.

Cornillon, P., and D. R. Watts, Satellite thermal infrared and

inverted echo sounder determinations of the Gulf Stream northern edge, *J. Atmos. Oceanic Technol.*, *4*, 712–723, 1987.

Derber, J., and A. Rosati, A global oceanic data assimilation system, *J. Phys. Oceanogr.*, *19*, 1333–1347, 1989.

Galperin, B., and G. L. Mellor, A time-dependent, three-dimensional model of the Delaware Bay and River, 1, Description of the model and tidal analysis, *Estuarine Coastal Shelf Sci.*, *31*, 231–253, 1990*a*.

Galperin, B., and G. L. Mellor, A time-dependent, three-dimensional model of the Delaware Bay and River, 2, Three-dimensional flow fields and residual circulation, *Estuarine Coastal Shelf Sci.*, *31*, 255–281, 1990*b*.

Gustafsson, N., A review of methods for objective analysis, in *Dynamic Meteorology: Data Assimilation Methods*, vol. 36, edited by L. Bengtsson, M. Ghil, and E. Kallen, pp. 17–76, Springer-Verlag, New York, 1981.

Hogg, N. G., R. S. Pickart, R. M. Hendry, and W. J. Smethie, The northern recirculation gyre of the Gulf Stream, *Deep Sea Res.*, *33*, 1139–1165, 1986.

Holland, W. R., and P. Malanotte-Rizzoli, Assimilation of altimeter data into an ocean circulation model: Space versus time resolution studies, *J. Phys. Oceanogr.*, *19*, 1507–1534, 1989.

Kantha, L. H., H. J. Herring, and G. L. Mellor, South Atlantic Bight OCS circulation model, *Rep. 91*, 154 pp., Dynalysis of Princeton, Princeton, N. J., 1986.

Kindle, J. C., Sampling strategies and model assimilation of altimetric data for ocean monitoring and prediction, *J. Geophys. Res.*, *91*, 2418–2432, 1986.

Leaman, K. D., R. L. Molinari, and P. S. Vertes, Structure and variability of the Florida Current at 27°N: April 1982–July 1984, *J. Phys. Oceanogr.*, *17*, 565–583, 1987.

Malanotte-Rizzoli, P., R. E. Young, and D. B. Haidvogel, Initialization and data assimilation experiments with primitive equation model, *Dyn. Atmos. Oceans*, *13*, 349–378, 1989.

Mellor, G. L., and A. F. Blumberg, Modeling vertical and horizontal diffusivities with the sigma coordinate system, *Mon. Weather Rev.*, *113*, 1279–1383, 1985.

Mellor, G. L., and T. Yamada, Development of a turbulent closure model for geophysical fluid problems, *Rev. Geophys.*, *20*, 851–875, 1982.

Mellor, G. L., C. Mechoso, and E. Keto, A diagnostic calculation of the general circulation of the Atlantic Ocean, *Deep Sea Res.*, *29*, 1171–1192, 1982.

Oey, L.-Y., G. L. Mellor, and R. I. Hires, A three-dimensional simulation of the Hudson-Raritan estuary, I, Description of the model and model simulations, *J. Phys. Oceanogr.*, *15*, 1676–1692, 1985*a*.

Oey, L.-Y., G. L. Mellor, and R. I. Hires, A three-dimensional simulation of the Hudson-Raritan estuary, II, Comparison with observation, *J. Phys. Oceanogr.*, *15*, 1693–1709, 1985*b*.

Richardson, P. L., Eddy kinetic energy in the North Atlantic from surface drifters, *J. Geophys. Res.*, *88*, 4355–4367, 1983.

Richardson, P. L., Average velocity and transport of the Gulf Stream near 55W, *J. Mar. Res.*, *43*, 83–111, 1985.

Robinson, A. R., M. A. Spall, and N. Pinardi, Gulf Stream simulations and the dynamics of ring and meander processes, *J. Phys. Oceanogr.*, *18*, 1811–1853, 1988.

Robinson, A. R., M. A. Spall, L. J. Walstad, and W. G. Leslie, Data assimilation and dynamical interpolation in Gulfcast experiments, *Dyn. Atmos. Oceans*, *13*, 301–316, 1989.

Shum, C. R., R. A. Warner, D. T. Sandwell, B. H. Zhang, R. S. Nerem, and B. D. Tapley, Variations of global mesoscale eddy energy observed from Geosat, *J. Geophys. Res.*, *95*, 17,865–17,876, 1990.

Spall, M. A., and A. R. Robinson, Regional primitive equation studies of the Gulf Stream meander and ring formation region, *J. Phys. Oceanogr.*, *20*, 985–1016, 1990.

Thompson, J. D., and W. J. Schmitz, A limited-area model of the Gulf Stream: Design, initial experiments, and model-data intercomparison, *J. Phys. Oceanogr.*, *19*, 791–814, 1989.

Verron, J., Altimeter data assimilation into an ocean circulation model: Sensitivity to orbital parameters, *J. Geophys. Res.*, *95*, 11,443–11,459, 1990.

White, W. B., C.-K. Tai, and W. R. Holland, Continuous assimilation of simulated Geosat altimetric sea level into an eddy-

—

resolving numerical ocean model, 1, Sea level differences, *J. Geophys. Res.*, *95*, 3219–3234, 1990*a*.

White, W. B., C.-K. Tai, and W. R. Holland, Continuous assimilation of simulated Geosat altimetric sea level into an eddy-resolving numerical ocean model, 2, Referenced sea level differences, *J. Geophys. Res.*, *95*, 3235–3252, 1990*b*.

White, W. B., C.-K. Tai, and W. R. Holland, Continuous assimilation of Geosat altimetric sea level observations into a numerical synoptic ocean model of the California Current, *J. Geophys. Res.*, *95*, 3127–3148, 1990*c*.

Willebrand, J., R. H. Kase, D. Stammer, H.-H. Hinrichsen, and W. Krauss, Verification of Geosat sea surface topography in the Gulf stream extension with surface drifting buoys and hydrographic measurements, *J. Geophys. Res.*, *95*, 3007–3014, 1990.

T. Ezer and G. L. Mellor, Program in Atmospheric and Oceanic Sciences, P. O. Box CN710, Sayre Hall, Princeton University, Princeton, NJ 08544.